Research Article

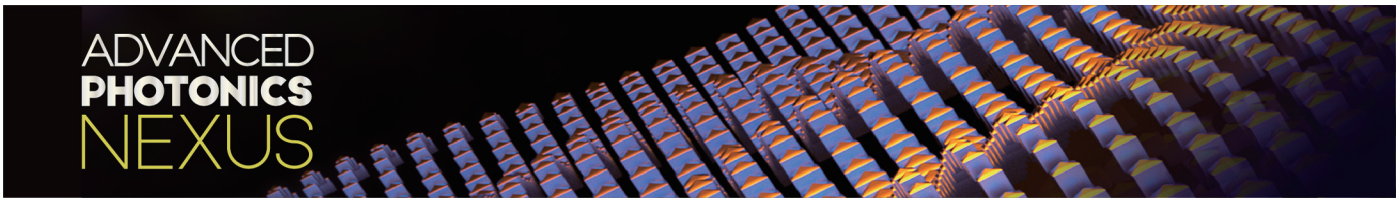

Digital subcarrier multiplexing-enabled carrier-free phase-retrieval receiver

Yunhe Ma, Meng Xiang,* Wenzhuo Cheng, Ruitao Wu, Peijian Zhou, Gai Zhou, Jilong Li, Jianping Li, Songnian Fu, and Yuwen Qin

Guangdong University of Technology, Department of Information Engineering, Guangdong Provincial Key Laboratory of Photonics Information Technology, Guangzhou, China

Abstract. The carrier-free phase-retrieval (CF-PR) receiver can reconstruct the optical field information only from two de-correlated intensity measurements without the involvement of a continuous-wave optical carrier. Here, we propose a digital subcarrier multiplexing (DSM)-enabled CF-PR receiver with hardware-efficient and modulation format-transparent merits. By numerically retrieving the optical field information of 56 GBaud DSM signals with QPSK/16QAM/32QAM modulation after 80-km standard single-mode fiber (SSMF) transmission, we identify that the DSM enabled CF-PR receiver is beneficial in reducing the implementation complexity of the CF-PR process, in comparison with the traditional single-carrier counterpart, because the lower symbol rate of each subcarrier is helpful in reducing the implementation complexity of multiple chromatic dispersion compensations and emulations during the PR iteration. Moreover, the DSM-enabled CF-PR receiver is verified to be robust toward various transmission imperfections, including transmitter-side laser linewidth and its wavelength drift, receiver-side time skew, and amplitude imbalance between two intensity tributaries. Finally, the superiority of the DSM-enabled CF-PR receiver is experimentally verified by recovering the optical field information of 25 GBaud 16QAM signals, after 40-km SSMF transmission for the first time. Thus, the DSM-enabled CF-PR receiver is promising for high-capacity photonic interconnection with direct detection.

Keywords: phase-retrieval; optical communications; direct detection; digital subcarrier multiplexing.

Received Jan. 13, 2023; revised manuscript received Mar. 3, 2023; accepted for publication May 16, 2023; published online Jun. 9, 2023.

[DOI: 10.1117/1.APN.2.4.046004]

1 Introduction

Optical field reconstruction, including both intensity and phase information, has been a long-standing issue in many fields of physics and their applications. Generally, coherent detection has been commonly used to recover the optical field in optical communications with the help of a local oscillator (LO) laser. Thus, both the use of complex modulation formats and the mitigation of various transmission impairments arising in the standard single-mode fiber (SSMF), such as chromatic dispersion (CD) and polarization mode dispersion (PMD), become realistic,[1–3] whereas the coherent detection receiver usually includes a high-power and wavelength-stabilized LO, an optical hybrid, and two pairs of balanced photodiodes (BPDs), making its overall cost and power consumption relatively high in comparison with its direct detection counterpart. Unfortunately, the loss of phase information is the major hurdle for direct detection, leading to an SSMF reach constraint for the high-speed intensity modulation direct detection (IM-DD) transmission. To bridge the gap between direct and coherent detection via combining the high-performance coherent transmission and the cost-effective direct detection, several self-coherent receivers have attracted worldwide research interest, such as the Kramers–Kronig (KK) receiver,[4,5] the carrier-assisted differential detection (CADD) receiver,[6,7] and the asymmetric self-coherent detection (ASCD) receiver.[8] Those self-coherent receivers utilize an additional continuous-wave (CW) optical carrier to co-propagate with the modulated optical signal at the transmitter side (Tx). Consequently, the optical field of modulation signals can be reconstructed from the term of carrier-signal beating after

*Address all correspondence to Meng Xiang, meng.xiang@gdut.edu.cn

direct detection. However, the signal-signal beating interference (SSBI) becomes the dominant constraint for those self-coherent receivers. Although the KK receiver can suppress the SSBI via the KK relation, the optical signal is restricted to the single-sideband (SSB) modulation to satisfy the minimum phase condition, at the expense of sacrificing half of the electrical spectral efficiency (ESE).[9] The CADD receiver can reconstruct the optical field with double-sideband (DSB) modulation for the purpose of ESE doubling, but the SSBI is eliminated because of its use of additional optoelectronic devices. Consequently, five photodiodes (PDs) and an optical hybrid are indispensable for the CADD receiver, leading to a complex hardware configuration. As for the ASCD receiver, the SSBI cancellation raises a stringent requirement on the sharp response of optical filter used. Furthermore, the carrier-to-signal-power ratio (CSPR), defined as a power ratio between the CW carrier and the modulated signal, has an individual value of at least 6, 7, and 10 dB for the KK, CADD, and ASCD receivers. However, such a high CSPR will limit the number of wavelength channels, due to the saturation of erbium-doped fiber amplifiers (EDFAs).

To circumvent the requirement of a strong CW optical carrier, a carrier-free phase-retrieval (CF-PR) receiver has been proposed to reconstruct the full optical field of the DSB signal via the intensity-only measurements of different projections. Then, a PR algorithm, such as the modified Gerchberg–Saxton (GS) algorithm, runs iteratively, until the numerically reconstructed intensities at all projection planes match the measurements. In terms of recovering quadrature amplitude modulation (QAM) signals, the CF-PR receiver has the simplest hardware configuration, including an optical splitter, a dispersive element, two single-ended PDs, and two-channel analog-to-digital converters (ADCs), in comparison with the CADD and ASCD receivers. However, the CF-PR receiver based on the modified GS algorithm usually suffers from slow convergency and the stagnant issue. Normally, around 1000 iterations are essential to approach a steady PR performance for the quadrature phase-shift keying (QPSK) signal.[10] The use of more intensity measurements is helpful to improve the PR performance with fewer iterations and steady bit error ratio (BER) at the cost of additional utilization of PDs and dispersion elements. The required number of iterations can be reduced to around 500 by utilizing three intensity measurements for the QPSK signal.[11] Alternatively, a PR receiver variant by adding a CW optical carrier, for the ease of PR initialization, has been investigated to realize the effective PR acceleration.[12–14] However, such a carrier-assisted PR scheme will not only sacrifice the spectral efficiency due to the optical carrier padding, but also require a CSPR of 5 dB. To pursue a faster and better convergency without sacrificing hardware resources, a CF-PR receiver with the use of symbol-wise GS error for the phase reset, which is denoted as PR_PR receiver, has been proposed.[11,15] It can experimentally realize a fast convergency with fewer than 500 iterations to reconstruct the 30 GBaud QPSK signals after 55-km SSMF transmission.[11] To further improve both the convergency speed and PR accuracy, we have proposed a CF-PR receiver with the aid of adaptive intensity transformation (AIT), which is denoted as a PR_AIT receiver.[16] It is numerically verified to accurately reconstruct the 56 GBaud QPSK signal after the 80-km SSMF transmission with the smallest 50 iterations so far. Generally speaking, the implementation complexity of the CF-PR receiver is determined by the PR algorithm, in terms of both the total number of iterations and the calculation complexity of each PR iteration. Until now, many research efforts have been devoted to cutting down the total number of iterations. However, how to reduce the calculation complexity of each PR iteration introduced by the multiple CD compensation (CDC) and emulation (CDE) is still an open question. Moreover, the CF-PR receiver is susceptible to being trapped into a local minimum instead of the global minimum when complex modulation formats are involved. Therefore, existing research on the CF-PR receiver has been mainly focused on simple modulation format, such as QPSK. Meanwhile, the experimental verification of CF-FR receiver for 16QAM has not yet been reported.

In this work, we propose a digital subcarrier multiplexing (DSM)-enabled CF-PR receiver, with hardware-efficient and modulation format-transparent merits. We identify that the DSM-enabled CF-FR receiver outperforms the conventional single-carrier counterpart when various modulation formats are employed by significantly reducing the implementation complexity of each PR iteration. Moreover, the DSM-enabled CF-PR receiver is helpful to enhance the robust operation towards various transmission impairments, including Tx laser linewidth and wavelength drift, Rx time skew, and the imbalance between two intensity tributaries. This paper is organized as follows. In Sec. 2, we introduce the generation of DSM signals at Tx and the corresponding operation principle of DSM-enabled CF-PR receiver. The simulation setup and comprehensive comparison between traditional single-carrier- and DSM-enabled CF-PR receivers are presented in Sec. 3. In Sec. 4, we carry out experimental verification for the DSM-enabled CF-PR receiver. Finally, we summarize our conclusion in Sec. 5.

2 Operation Principle

2.1 Generation of DSM Signals

The DSM technique is based on dividing a high baud-rate single-carrier signal into multiple lower baud-rate subcarrier signals, which has been extensively explored in coherent fiber optical transmission systems.[17–22] For the generation of conventional single-carrier signals, a sequence of QAM symbols is first generated after the bit-to-symbol mapping, then up-sampled to two samples per symbol (Sps) and spectrally shaped by a root-raised cosine (RRC) filter in the frequency domain with a roll-off factor of α. As for the generation of DSM signals shown in Fig. 1, a sequence of QAM symbols is first generated after the bit-to-symbol mapping and then divided into M streams, where M is the number of subcarriers. After symbols are upsampled to two Sps for each subcarrier, those samples are transformed to the frequency domain and spectrally filtered by an RRC filter with a roll-off factor of α. Next, those outputs are upsampled by M in the frequency domain with zero padding, shifted to corresponding subcarrier position, and digitally multiplexed. As we can see, since no guard band is reserved among subcarriers for the DSM signal, the optical bandwidth and the SE are the same as that of the single-carrier signal. Actually, the single-carrier signal can be regarded as a special DSM signal, under the condition of $M = 1$.

2.2 DSM-Enabled CF-PR Receiver

The objective of the CF-PR receiver is to reconstruct the optical field of QAM signals from two intensity measurements, $|s(t)|^2$

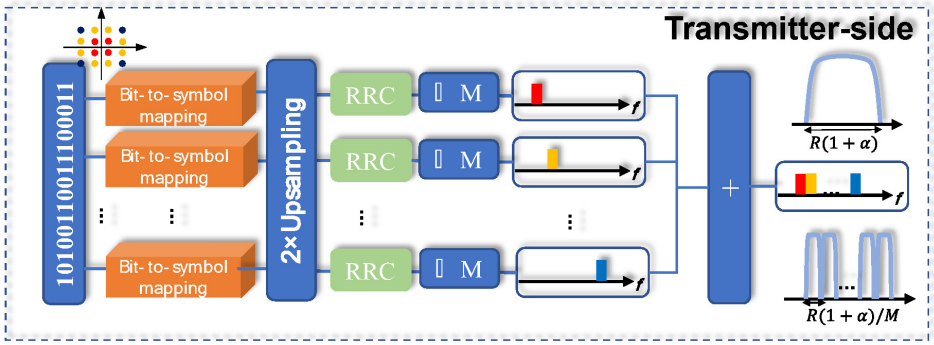

Fig. 1 Generation of DSM signals at Tx.

and $|d(t)|^2$, where $s(t)$ and $d(t)$ are the undispersed signal and the dispersed signal, respectively. We set $a(t) = |s(t)|$ and $b(t) = |d(t)|$ for the ease of discussion. The solution for the reconstruction of the optical field can be represented as a problem of identifying a phase signal $\angle\hat{s}(t)$ to satisfy the following equation:

$$\arg\min_{\angle\hat{s}(t)} \sum_{m=1}^{P} \left\{ \left| \sum_{k} a(k) \exp[j\angle\hat{s}(t)] \cdot h_D(mT - kT) \right| - b(mT) \right\}^2, \tag{1}$$

where $h_D(t)$ is the complex transfer function introduced by the use of the dispersive element, and T is the symbol duration. The process of identifying the value of $\angle\hat{s}(t)$ that minimizes Eq. (1) is realized by the iterative PR algorithm with several physical constraints. To enhance the CF-PR performance, we propose applying the DSM instead of the more commonly used single-carrier modulation for the CF-PR receiver. In addition, we apply the PR_AIT algorithm for recovering the QAM signals, as summarized in Table 1, where h_{CD} represents the CD transfer function of the fiber transmission. $I_{\max}$ is the maximal number of iterations for the PR_AIT algorithm. h_{RRC} is the RRC shaping filter. t'_p is the time slot assigned for pilot symbols x_p, and $\otimes$ represents the convolution operation. As for the PR process, a random phase ranging from $-\pi$ to π is initialized, and the retrieved phase is updated after every iteration. Within the iteration loop, the measured intensity is first powered by a factor of P, which is adaptively adjusted with respect to the current iteration by a maximal powering factor R and a decaying factor V.[16] Then, the reconstructed DSM signal is propagated back to the Tx by imposing the CDC function of h_{CD}^{-1}, along with the subcarrier demultiplexing. To reduce the implementation complexity, the CDC and the subcarrier demultiplexing are implemented in the frequency domain. After passing through an RRC filter and being downsampled to one Sps for each subcarrier, the pilot constraint is implemented to update the phase of the samples at the predetermined location.[10] Note that the RRC shaping can be merged into CDC in the frequency domain. Thereafter, the electrical signal for each subcarrier is upsampled to two Sps, RRC-shaped, and finally subcarrier-multiplexed. After further propagating to the projection plane, the signal intensity is replaced with the transformed intensity. Again, the propagation of DSM signals is implemented in the frequency domain. Then the signal phase is correspondingly updated for the next iteration.

3 Simulation Results and Discussions

3.1 Simulation Setup

To examine the performance of the proposed DSM-enabled CF-PR receiver, we carry out numerical simulations for single-polarization QPSK/16QAM/32QAM signals. The simulation setup and the corresponding DSP stack are shown in Fig. 2. The RRC-shaped DSM signals are first generated offline with an aggregate baud rate of 56 GBaud, as shown in the following equation:

$$S(t) = \sum_{k=1}^{M} \sum_{m=-\infty}^{\infty} [S_k(m) h_{\mathrm{RRC}}(t - mT) \exp(j2\pi f_k t)], \quad M = 1, 2, 4, \ldots, \tag{2}$$

where S_k represents the information carried by the k'th subcarrier, and f_k is the subcarrier position for the k'th subcarrier

Table 1 PR_AIT algorithm for DSM signals.

Function $a(t), b(t), R, V, h_{\mathrm{CD}}, h_D, I_{\max}$

1. $\angle\hat{s}(t) = \angle\mathrm{rand}(t)$ ◇ Initialize phase
2. **For** i **from** 1 **to** $I_{\max}$
3. $a(t) \leftarrow a(t)^P$, $b(t) \leftarrow b(t)^P$; where $P = (R-1) \cdot \exp(-i/V) + 1$ ◇ AIT
4. $\hat{s}(t) = a(t) \exp(j\angle\hat{s}(t))$ ◇ Reconstruct the field
5. $\hat{s}(t) \leftarrow h_{\mathrm{CD}}^{-1}(t) \otimes \hat{s}(t)$ ◇ Propagate back to Tx
6. $\hat{s}_k(t) \leftarrow \hat{s}(t)$ ◇ Subcarrier demultiplexing
7. $\hat{s}_k(t) \leftarrow h_{\mathrm{RRC}}(t) \otimes \hat{s}_k(t)$ ◇ RRC shaping
8. $\hat{s}_k(t') \leftarrow \hat{s}_k(t)$ ◇ Downsample to one Sps
9. $\hat{s}_k(t'_p) \leftarrow |s_p(t'_p)| \exp[j\angle s_p(t'_p)]$ ◇ Pilot constraint
10. $\hat{s}_k(t) \leftarrow \hat{s}_k(t')$ ◇ Upsample to two Sps
11. $\hat{s}_k(t) \leftarrow h_{\mathrm{RRC}}(t) \otimes \hat{s}_k(t)$ ◇ RRC shaping
12. $\hat{s}(t) \leftarrow \hat{s}_k(t)$ ◇ Subcarrier multiplexing
13. $\hat{s}(t) \leftarrow h_{\mathrm{CD}}(t) \otimes h_D(t) \otimes \hat{s}(t)$ ◇ To projection plane
14. $\hat{s}(t) \leftarrow b(t) \exp[j\angle\hat{s}(t)]$ ◇ Intensity update
15. $\hat{s}(t) \leftarrow h_D^{-1}(t) \otimes \hat{s}(t)$ ◇ Propagate back to Rx
16. **Returns** $\exp[j\angle\hat{s}(t)]$

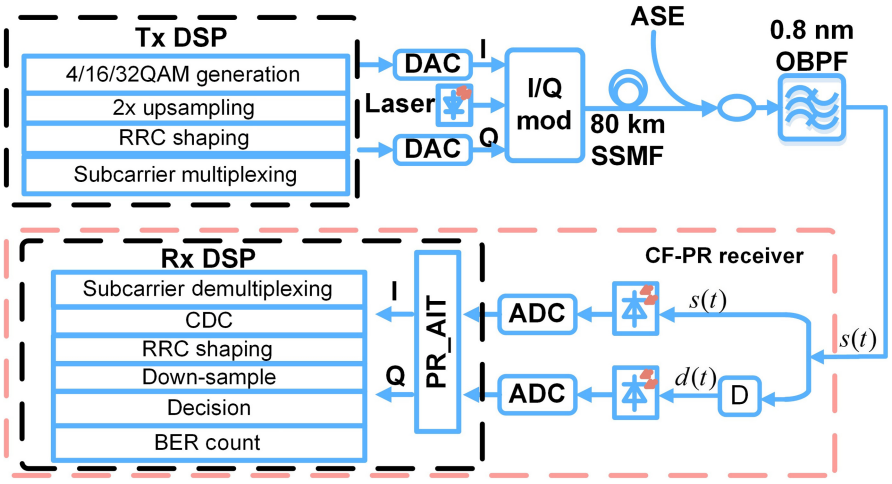

Fig. 2 Simulation setup and corresponding DSP stack.

signal. During our investigation, the roll-off factor of the RRC shaping is fixed at 0.01. Then the digital signals are converted to the analog signals via two digital-to-analog converters (DACs) and further drive the IQ modulator for generating the optical QAM signal. The 1550-nm semiconductor laser with a linewidth of 100 kHz is chosen as the laser source. Two DACs operate at a sampling rate of 112 GSa/s with a resolution of 8 bits.

The transmission link includes a span of 80-km SSMF with a CD parameter of 17 ps/nm/km. We ignore the nonlinearity induced by the SSMF for simplicity. After the SSMF transmission, a noise-loading module is used to adjust the optical signal-to-noise ratio (OSNR) of received signals. After passing through an optical bandpass filter (OBPF) with a 3-dB bandwidth of 100 GHz, the signal is fed into the CF-PR receiver, including an optical splitter, a dispersive element, two single-ended PDs, whose response is emulated as a fourth-order Bessel filter with a 3-dB bandwidth of 60 GHz, and two ADCs with a resolution of 8 bits and a sampling rate of 160 GSa/s. Once the optical field reconstruction is realized by the PR_AIT algorithm, the following Rx DSP flow for the DSM signals first begins with the subcarrier demultiplexing, CDC, and the matched RRC filtering. Afterwards, the downsampling to one Sps and the symbol decision are implemented under the subcarrier basis. Finally, we calculate the BER for each subcarrier and record the averaged BER for the DSM signals.

3.2 PR Performance Comparison

First, we investigate the effect of the dispersive element on the performance of the DSM-enabled CF-PR receiver, under the condition of 19, 27, and 33 dB OSNR for QPSK/16QAM/32QAM signals, respectively. The CF-PR receiver with traditional single-carrier modulation is presented, for ease of fair comparison.[16] The achieved BER with respect to the CD value of the dispersive element is summarized in Fig. 3. The total number of iterations is set to 500 to ensure full convergence, and 20% periodically inserted pilot symbols are used. We find that the PR performance improves with the growing CD value due to the involvement of more symbols. We credit such a phenomenon to the fact that the introduction of a large CD is helpful to decorrelate two intensity measurements and prevent the PR_AIT algorithm from being trapped into a suboptimal solution. Moreover, the BER starts to saturate, after the use of a sufficiently large amount of CD. The minimum CD value required to ensure optimal PR performance is found to be 4500 ps/nm. For ease of discussion, we fix the CD value of the dispersive element at 4500 ps/nm for next investigations. In particular, the BER performance is almost the same for single-carrier- and DSM-enabled CF-PR receivers under various CD values.

Next, we investigate the BER performance with respect to various OSNRs for the single carrier- and the DSM-enabled

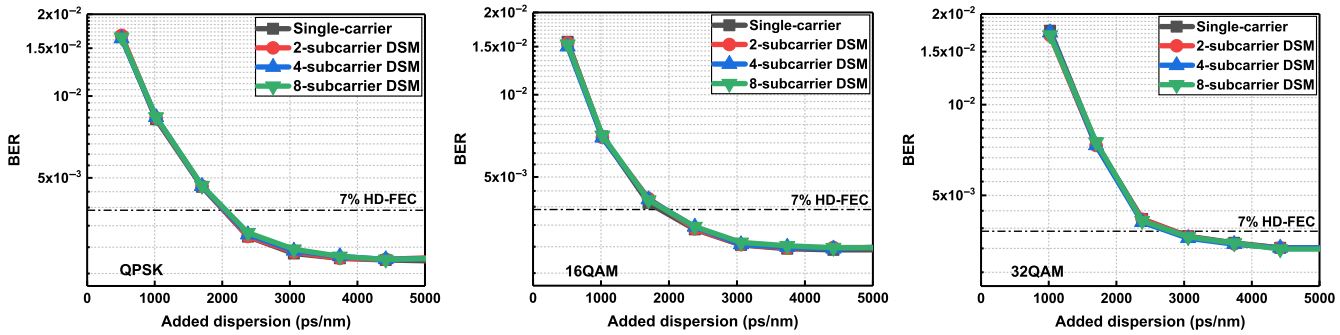

Fig. 3 Simulated BER with respect to the dispersion of dispersion element used when the modulation format is (a) QPSK, (b) 16QAM, and (c) 32QAM.

CF-PR receivers; the theoretical performance is also included for the purpose of comparison. As shown in Fig. 4, the BER performance becomes better along with the growing OSNR. Again, the BER performance is almost the same for single-carrier- and DSM-enabled CF-PR receivers, after the convergency. However, both the single-carrier- and DSM-enabled CF-PR receivers experience a performance penalty in comparison with the theory curve. To reach the threshold of 7% hard-decision FEC (HD-FEC) at BER $= 3.8 \times 10^{-3}$, the required OSNRs for 56 GBaud QPSK/16QAM/32QAM signals are 18.5, 26.2, and 32.4 dB, respectively.

To investigate the performance of the convergence speed, we investigate the BER performance with respect to the number of iterations, as shown in Fig. 5, under the condition of 19, 27, and 33 dB OSNR for QPSK/16QAM/32QAM signals, respectively. The BER performance becomes better with the growing number of iterations and is finally saturated to a steady value. Note that an optimal number of iterations occur, which are determined by the AIT parameters and OSNR as a result of the interaction between the noise and intensity signal when the PR_AIT algorithm is applied.[16] Similarly, the single-carrier- and DSM-enabled CF-PR receivers have the same BER performance under various numbers of iterations, revealing that both CF-PR receivers have the same convergency speed.

3.3 Tolerance of Transmission Impairments

Intuitively, the phase noise induced by the laser linewidth is inessential during the intensity measurements, without impact on the PR performance. For the first time, we investigate the impact of phase noise on the PR performance by tuning the Tx laser linewidth. When the required OSNR without phase noise is considered as the benchmark, the required OSNR penalty with respect to the laser linewidth is summarized in Fig. 6. The PR performance is quite susceptible to the phase noise, because the interaction between phase noise and CD generates the phase-to-amplitude conversion noise.[23] In addition, the required OSNR penalty becomes larger along with the use of higher-order QAM, because the higher-order QAM is sensitive to the noise. However, we find that, the DSM-enabled CF-PR receiver has a better tolerance toward phase noise because the DSM signals have less CD-induced impairment.[24,25] The larger number of subcarriers we set, the better the PR performance can be always guaranteed under sufficiently large linewidth.

Since the uncooled lasers are preferred for the reduction of power consumption, the operation wavelength of the laser may vary with respect to the time and environment. Such a wavelength drift further worsens the CD-induced phase distortions, which are proportional to the square of laser wavelength,[26] as shown in the following equation:

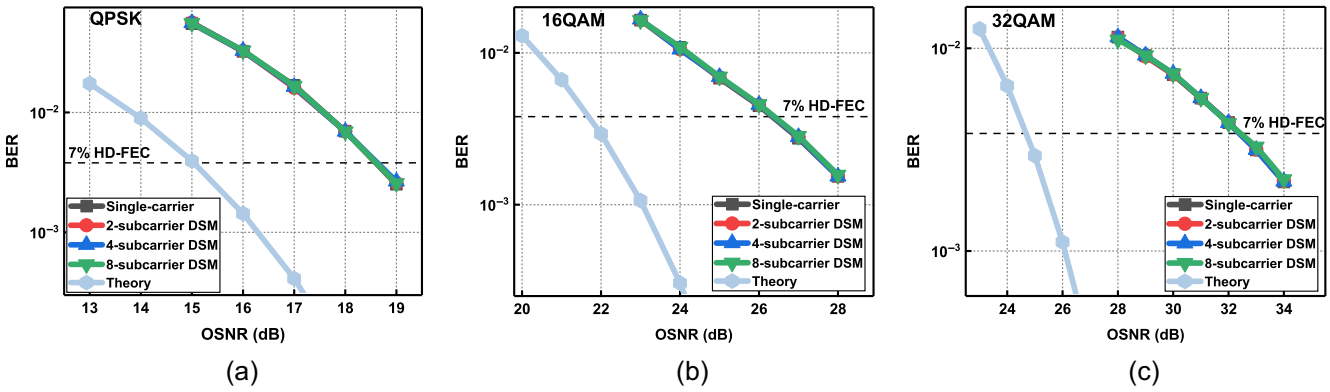

Fig. 4 Simulated BER with respect to the OSNR of received signals when the modulation format is (a) QPSK; (b) 16QAM; (c) 32QAM.

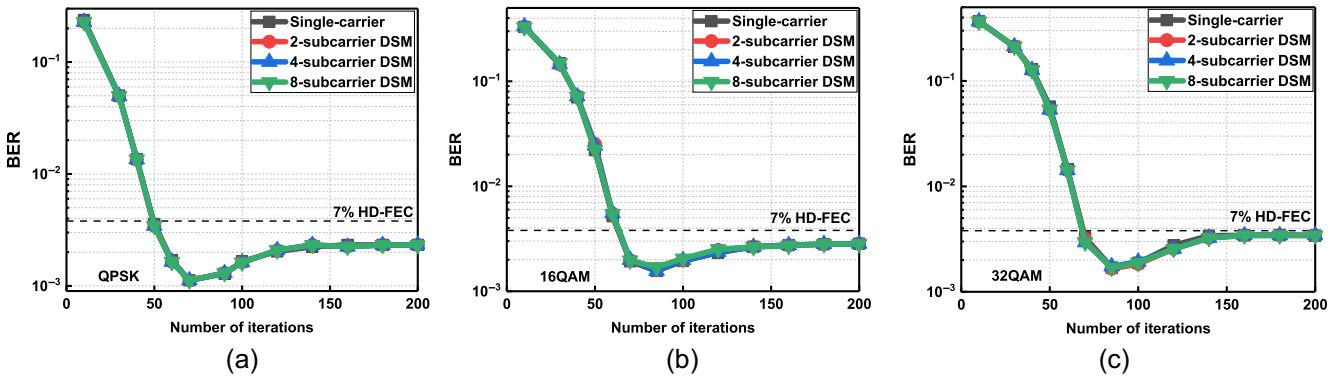

Fig. 5 Simulated BER as a function of iteration when the modulation format is (a) QPSK; (b) 16QAM; (c) 32QAM.

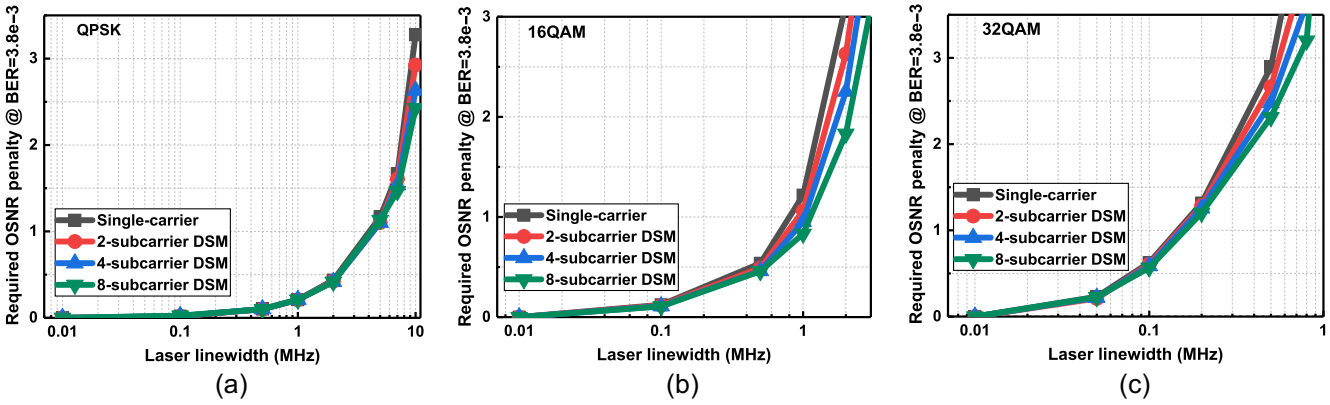

Fig. 6 Simulated tolerance toward the laser linewidth when the modulation format is (a) QPSK; (b) 16QAM; (c) 32QAM.

$$H(f) = \exp(-j\pi DLf^2\lambda^2/c), \tag{3}$$

where DL is the accumulated dispersion of SSMF or the dispersion element, and f, λ, and c are the analog frequency, laser central wavelength, and velocity of light, respectively. To investigate the tolerance of the CF-PR receiver against the wavelength drift, a fixed wavelength error to emulate the wavelength drift is added in Eq. (3), with the assumption that the central wavelength of the laser used is 1550 nm. The required OSNR without the wavelength drift is considered as the benchmark; the required OSNR penalty with respect to the wavelength drift is summarized in Fig. 7. The PR performance is sensitive to the wavelength drift, especially when the higher-order QAM is chosen. In addition, the utilization of DSM signals is helpful to enhance the tolerance of wavelength drift, as DSM signals are more robust to the CD-induced phase distortions. Given 1 dB required OSNR penalty, the wavelength drift tolerance of ± 2.02, ± 1.15, and ± 0.37 nm for the single-carrier-enabled CF-PR receiver can be obtained when QPSK/16QAM/32QAM modulation formats are employed, respectively. As for the DSM-enabled CF-PR receiver, the wavelength drift tolerance can be improved to ± 2.11, ± 1.37, and ± 0.48 nm for the eight-subcarrier QPSK/16QAM/32QAM modulation formats, respectively. To recap, the DSM-enabled CF-PR receiver is more robust to Tx laser imperfections, including both laser linewidth and wavelength drift, in comparison with the single-carrier-enabled CF-PR receiver.

Finally, we investigate the tolerance toward the imperfection of the CF-PR receiver, including the time skew and the amplitude imbalance between two tributary signals, $s(t)$ and $d(t)$. Note that we load additional noise to the signal $d(t)$ to emulate the amplitude imbalance after the amplitude normalization, which indeed results in an OSNR difference. Figures 8 and 9 show the required OSNR penalty for the signal $s(t)$ to reach the 7% HD-FEC threshold. Evidently, the PR performance degrades along with receiver imperfections for both the single-carrier- and DSM-enabled receivers. Considering 1 dB required OSNR penalty, the skew tolerance of 7.10, 3.37, and 1.43 ps is obtained for the single-carrier-enabled CF-PR receiver employing QPSK/16QAM/32QAM modulation, respectively, as shown in Fig. 8. Meanwhile, the skew tolerance can be enhanced to 7.43, 4.21, and 1.63 ps for the eight-subcarrier DSM-enabled CF-PR receiver utilizing QPSK/16QAM/32QAM modulation, respectively. The reason the DSM-enabled CF-PR receiver guarantees an improved skew tolerance is that the symbol duration of each subcarrier of DSM signals is much longer than that of the single-carrier signal. Similarly, the amplitude imbalance tolerance is found to be 2.40, 2.02, and 1.53 dB for the single-carrier-enabled CF-PR receiver with QPSK/16QAM/32QAM modulation, respectively. Alternatively, it

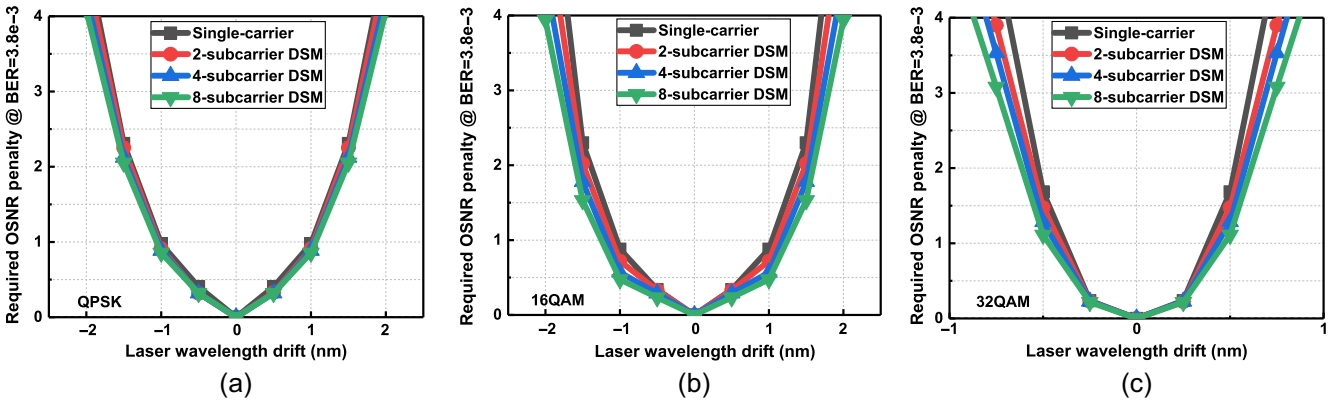

Fig. 7 Simulated tolerance toward the wavelength drift when the modulation format is (a) QPSK; (b) 16QAM; (c) 32QAM.

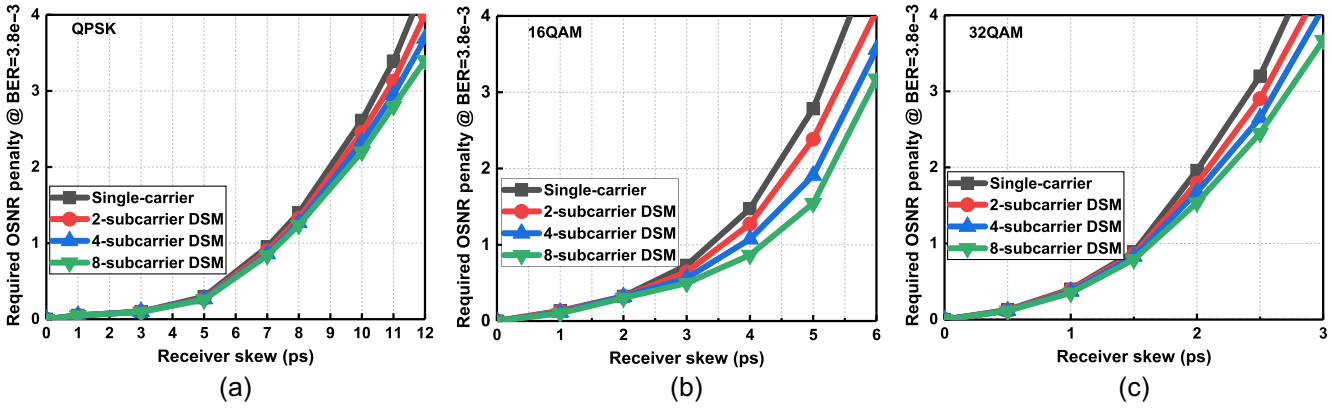

Fig. 8 Simulated tolerance toward the receiver skew when the modulation format is (a) QPSK; (b) 16QAM; (c) 32QAM.

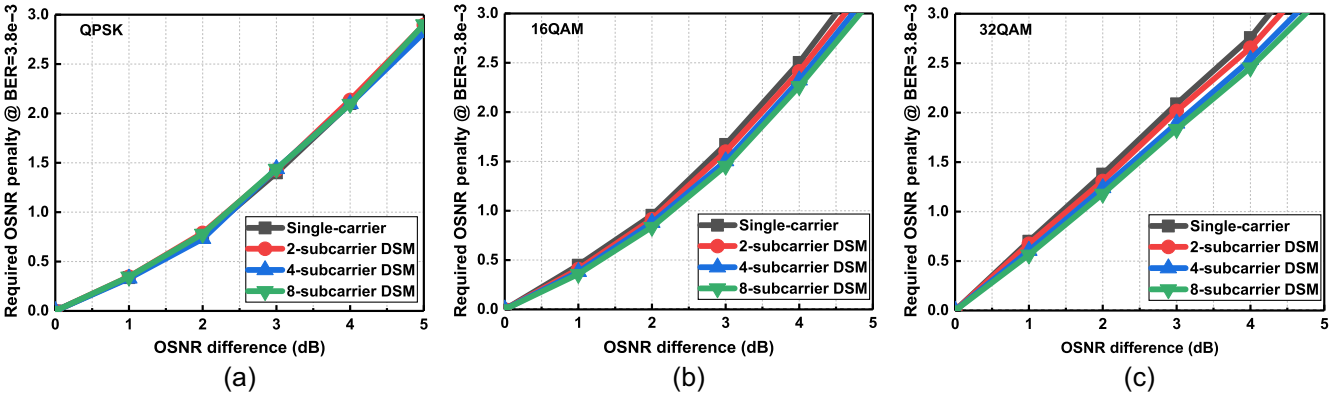

Fig. 9 Simulated tolerance toward the amplitude imbalance when the modulation format is (a) QPSK; (b) 16QAM; (c) 32QAM.

can be improved to 2.42, 2.33, and 1.71 dB for the eight-subcarrier DSM-enabled CF-PR receiver with QPSK/16QAM/32QAM modulation, respectively. Therefore, the DSM-enabled CF-PR receiver outperforms its traditional single-carrier counterpart in terms of the tolerance towards receiver-side imperfections. Although the PR_AIT algorithm is taken into account during our investigation, the same conclusion can be drawn for other CF-PR algorithms.

3.4 Comparison of Calculation Complexity

Since the calculation complexity of the CF-PR receiver is critical for the hardware implementation, it is essential to compare the single-carrier- and DSM-enabled CF-PR receivers. The PR_AIT algorithm is implemented in a block-wise manner with a block size of N and N/M for the single-carrier- and DSM-enabled receivers, respectively.[23–25] The received signals after the ADC is assumed to be with two Sps. The calculation complexity of the PR_AIT algorithm for the DSM-enabled receiver can be summarized as follows:

1. Assume the ADC has n-bits for quantization; then the quantized intensity signal has 2^n levels. Therefore, we can use a 1×2^n look-up-table (LUT) to store the signal levels after the transformation. Since the LUT contents can be calculated offline, it is assumed to be without hardware consumption.

2. Since the signal $a(t)$ is real, the reconstruction of the optical field in step 4 requires $2N/M$ real multiplications only.

3. Propagating back to Tx, subcarrier demultiplexing and RRC shaping from step 5 to step 7 can be executed within a single step in the frequency domain, using different sizes of fast Fourier transform (FFT)/inverse fast Fourier transformation (IFFT).[23,24] It requires $N/M \cdot \log_2(N/M)/2$ complex multiplications to execute FFT of N/M complex samples, and $N/M^2 \cdot \log_2(N/M^2)/2$ complex multiplications to execute IFFT of N/M^2 complex samples for each subcarrier. In addition, the filtering operation in frequency domain requires N/M complex multiplications for all subcarriers. Therefore, $N/M/2 \cdot [\log_2(N/M) + \log_2(N/M^2) + 2]$ complex multiplications are required from step 5 to step 7. Since a complex multiplication can be implemented using four real multiplications and two real adders, $N/M/2 \cdot [\log_2(N/M) + \log_2(N/M^2) + 2]$ complex multiplications equal to $2N/M \cdot [\log_2(N/M) + \log_2(N/M^2) + 2]$ real multiplications and $N/M \cdot [\log_2(N/M) + \log_2(N/M^2) + 2]$ real adders.

4. The downsampling in step 8 can be completed in the time domain by discarding half of the symbols without enhancing the implementation complexity.

5. Substituting symbols in specific positions with pilots in step 10 does not consume any multiplications and adders.

6. Similarly, the implementation of upsampling in step 10, RRC shaping in step 11, subcarrier multiplexing in step 12, and propagation to the projection plane in step 13 can be combined, requiring $2N/M \cdot [\log_2(N/M) + \log_2(N/M^2) + 2]$ real multiplications and $N/M \cdot [\log_2(N/M) + \log_2(N/M^2) + 2]$ real adders, respectively.

7. Intensity updating in step 14 requires $2N/M$ real multiplications.

8. Propagating back to the receiver side in step 15 requires $2N/M \cdot [\log_2(N/M) + \log_2(N/M^2) + 2]$ real multiplications and $N/M \cdot [\log_2(N/M) + \log_2(N/M^2) + 2]$ real adders, respectively.

9. Calculating $\exp[j\angle\hat{s}(t)]$ and forwarding it for the next iteration in step 16 requires $2N/M$ real multiplications.

Therefore, the AIT_PR algorithm for each iteration requires $6N \cdot [\log_2(N/M) + \log_2(N/M^2) + 3]$ real multiplications, $3N \cdot [\log_2(N/M) + \log_2(N/M^2) + 2]$ real adders, and a 1×2^n LUT for the DSM-enabled CF-PR receiver with M blocks (N samples in total), respectively. Since the block size N is determined by the accumulated CD from the fiber and dispersion element, we choose it to be 1024 by taking 50% overlapping frequency domain equalization into account. Therefore, we can obtain the calculation complexity of the PR_AIT algorithm, as shown in Fig. 10. The calculation complexity can be greatly reduced by the utilization of the DSM-enabled CF-PR receiver.

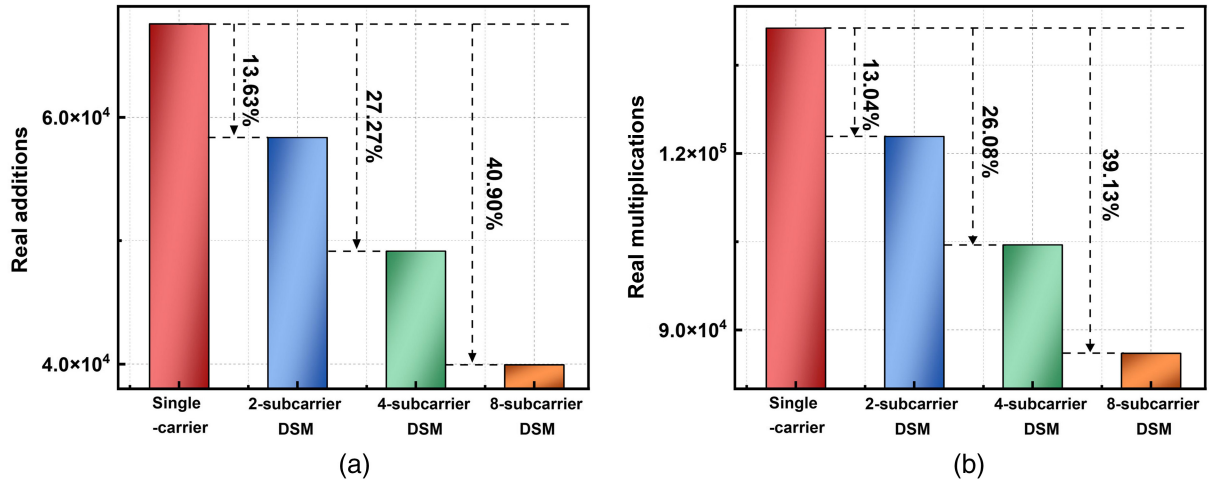

Fig. 10 Implementation complexity comparison, in terms of (a) number of adders and (b) number of multiplications.

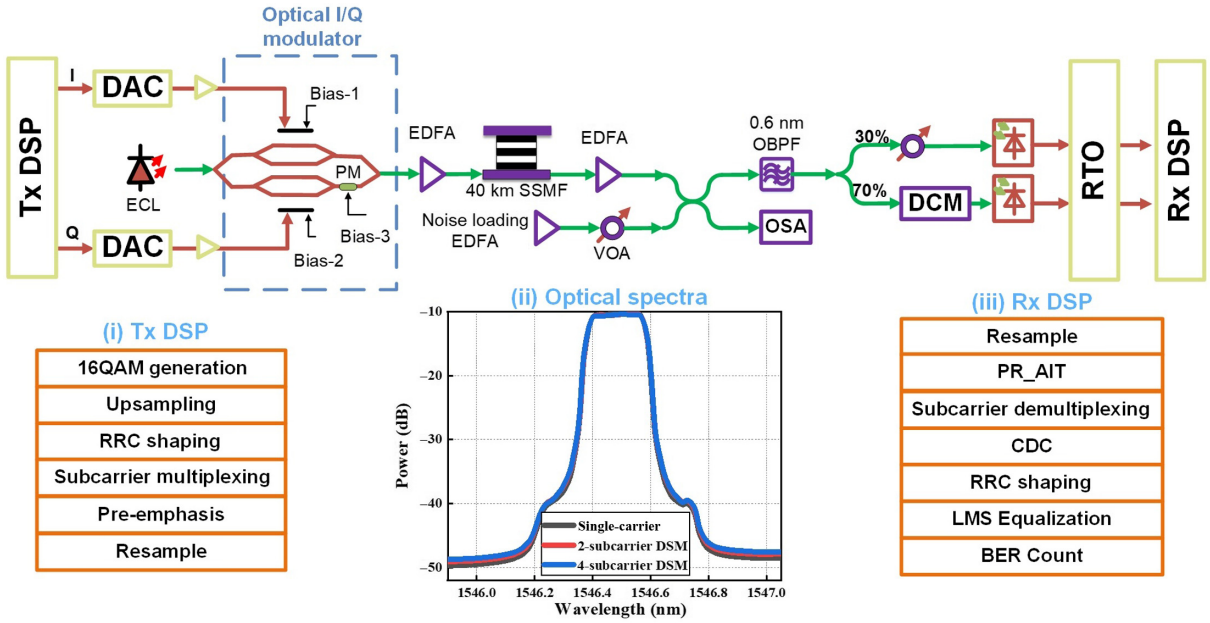

Fig. 11 Experimental setup of 25 GBaud 16QAM fiber optical transmission.

As for the eight-subcarrier DSM-enabled CF-PR receiver, we can reduce the calculation complexity by 39.13% and 40.90%, respectively, in terms of the real multiplications and real adders, in comparison with the single-carrier-enabled CF-PR receiver.

4 Experimental Results and Discussions

We carry out a proof-of-concept experimental verification, as shown in Fig. 11. A C-band external cavity laser with the central wavelength of 1546.4771 nm and a linewidth of less than 100 kHz is chosen as the laser source. At the Tx, the single-carrier and DSM 16QAM electrical signals are generated offline and filtered by an RRC filter with a roll-off factor of 0.01. Afterwards, a pre-emphasis module is applied to compensate for the spectral attenuation from the Tx. After the resampling, the signal is loaded into the arbitrary waveform generator (AWG) operated at 32 GS/s sampling rate with 8-bit resolution. The aggregate baud rate of the DSM signal is 25 GBaud, which is the same as that of single-carrier signals. Afterwards, the electrical signal is first amplified and then fed to the I/Q modulator for the electrical-to-optical conversion. The I/Q modulator output is boosted to 5.7 dBm by an EDFA, and then introduced into a span of 40 km SSMF.

At the Rx, the optical signal is first amplified to 24 dBm, and the noise loading is applied to manage the OSNR. Afterwards, the optical signal is filtered with an OBPF and then split into two parts with a 30:70 optical coupler. The 70% power tributary is dispersed by two cascaded dispersion compensation modules (DCMs) with a tunable CD value within the range from 0 to 2826 ps/nm. The total insertion loss of two cascaded DCMs is 8.5 dB. The received optical power of both the undispersed signal and the dispersed signal is ~5 dBm. Then, two optical signals are detected by two PDs and digitized by an 80 GS/s real-time oscilloscope. As for the Rx DSP, the signals are first resampled to two Sps, followed by the PR_AIT algorithm. Then, the reconstructed signal is fed to the CDC module, along with

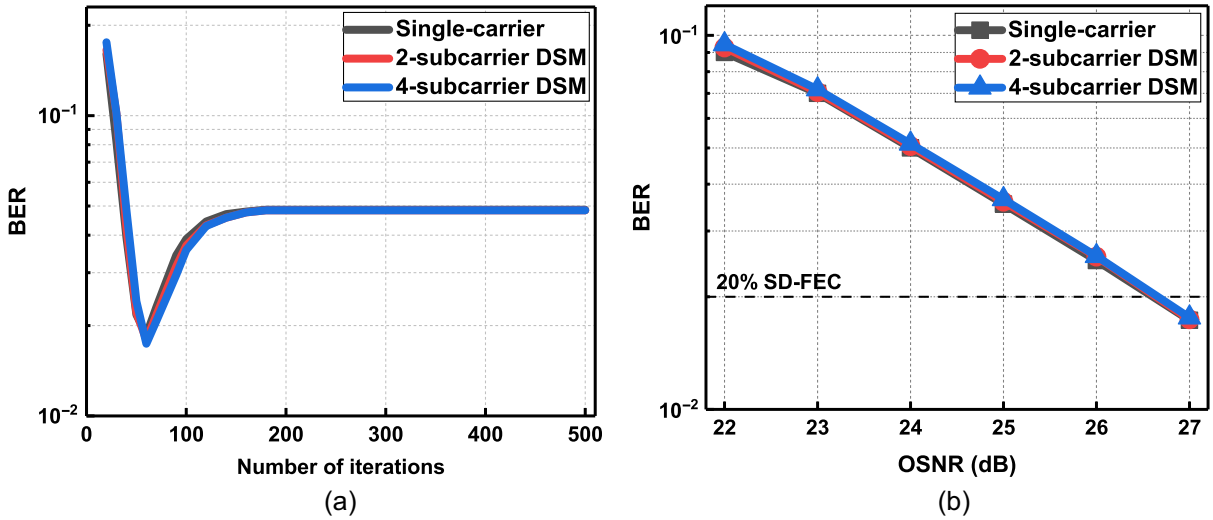

Fig. 12 Achieved BER as a function of (a) number of iterations and (b) OSNR.

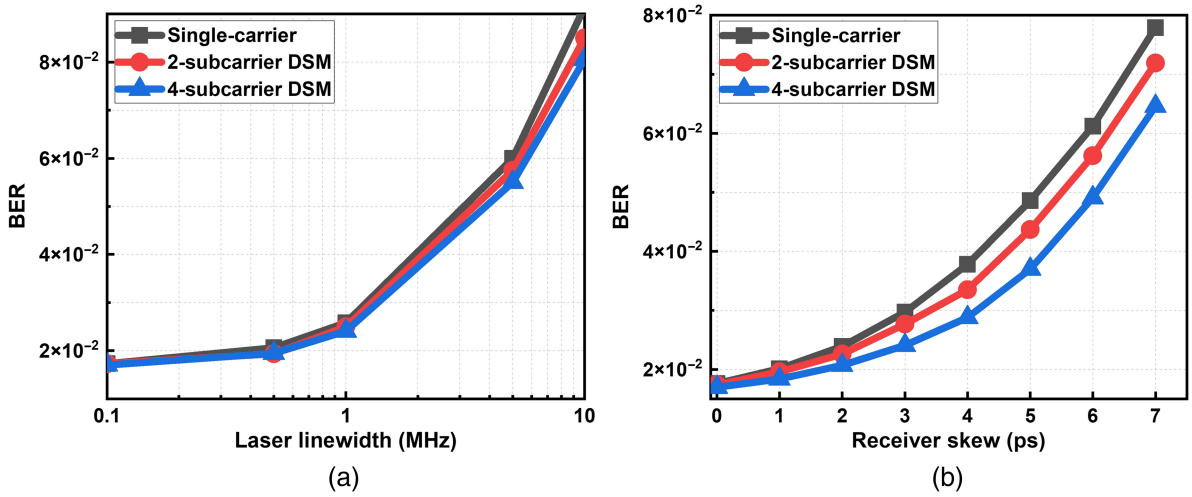

Fig. 13 Achieved BER as a function of (a) laser linewidth, and (b) receiver skew.

subcarrier demultiplexing and matched RRC filtering. Thereafter, a feedforward equalizer based on the least mean square algorithm is applied for each subcarrier before the symbol decision. Finally, we calculate the BER for ease of performance comparison.

We first investigate the convergency for the single-carrier- and DSM-enabled CF-PR receivers, as shown in Fig. 12(a). Obviously, the single-carrier- and DSM-enabled receivers have the same BER performance, under various number of iterations, indicating the same convergency speed. Additionally, the obtained BER for both receivers first decreases, then increases, and finally gets saturated along with increasing the number of iterations, which is consistent with that in simulations. To ensure the optimal performance, we fix the number of iterations at 60, to experimentally guarantee the optimal PR performance. We then investigate the BER performance with respect to the OSNR, as shown in Fig. 12(b). The obtained BER becomes gradually better along with the growing OSNR. Both the single-carrier- and DSM-enabled receivers show the same BER performance under various OSNRs. Therefore, the single-carrier- and DSM-enabled CF-PR receivers have the same PR performance in terms of convergency speed and steady BER performance.

Thereafter, the impact of laser linewidth on the CF-PR imperfections on the single-carrier- and DSM-enabled receivers is investigated. Note that we manually add phase noise in the digital domain after the pre-emphasis to emulate the tunable linewidth. Figure 13(a) summarizes the relationship between the laser linewidth and the BER under the condition of OSNR of 27 dB. The use of the DSM-enabled CF-PR receiver can enhance the tolerance toward the laser linewidth. Finally, we examine the impact of skew on the CF-PR receiver, as shown in Fig. 13(b). Similarly, better BER performance can be guaranteed for the DSM-enabled CF-PR receiver under the condition of variable skew.

5 Conclusion

We propose a DSM-enabled CF-PR receiver with both the reduction of implementation complexity and the transparent operation of modulation format. When the optical field of 56 GBaud QPSK/16QAM/32QAM signals is numerically reconstructed after 80-km SSMF transmission, we identify that the DSM-enabled CF-PR receiver outperforms its traditional single-carrier counterpart in terms of implementation complexity and the tolerance towards various transmission impairments, including the transmitter laser linewidth, the transmitter wavelength drift, the receiver skew, and the amplitude imbalance between two intensity measurements. Finally, we carry out the experimental demonstration of recovering 25 GBaud 16QAM signals after a 40-km SSMF transmission, verifying the superiority of the DSM-enabled CF-PR receiver.

Data Availability

Data underlying the results presented in this paper are not publicly available at this time but may be obtained from the authors upon reasonable request.

Acknowledgments

This work was partially supported by the National Key Research and Development Program of China (Grant No. 2021YFB2900702), the National Natural Science Foundation of China (Grant No. U21A20506), and the Guangdong Introducing Innovative and Entrepreneurial Teams of "The Pearl River Talent Recruitment Program" (Grant No. 2021ZT09X044). The authors declare no conflicts of interest.

References

1. R.-J. Essiambre et al., "Capacity limits of optical fiber networks," *J. Lightwave Technol.* **28**(4), 662–701 (2010).
2. E. Ip et al., "Coherent detection in optical fiber systems," *Opt. Express* **16**(2), 753–791 (2008).
3. K. Kikuchi, "Fundamentals of coherent optical fiber communications," *J. Lightwave Technol.* **34**(1), 157–179 (2016).
4. A. Mecozzi, C. Antonelli, and M. Shtaif, "Kramers–Kronig coherent receiver," *Optica* **3**(11), 1220–1227 (2016).
5. X. Chen et al., "Kramers–Kronig receivers for 100-km datacenter interconnects," *J. Lightwave Technol.* **36**(1), 79–89 (2018).
6. C. Sun et al., "Experimental demonstration of complex-valued DSB signal field recovery via direct detection," *IEEE Photonics Technol. Lett.* **32**(10), 585–588 (2020).
7. W. Shieh, C. Sun, and H. Ji, "Carrier-assisted differential detection," *Light. Sci Appl.* **9**, 18 (2020).
8. X. Li et al., "Asymmetric self-coherent detection based on Mach-Zehnder interferometers," *J. Lightwave Technol.* **40**(7), 2023–2032 (2022).
9. A. Mecozzi, C. Antonelli, and M. Shtaif, "Kramers–Kronig receivers," *Adv. Opt. Photonics* **11**(3), 480–517 (2019).
10. H. Chen et al., "Dual polarization full-field signal waveform reconstruction using intensity only measurements for coherent communications," *J. Lightwave Technol.* **38**(9), 2587–2597 (2020).
11. H. Chen et al., "Phase retrieval with fast convergence employing parallel alternative projections and phase reset for coherent communications," *Opt. Lett.* **45**(5), 1188–1191 (2020).
12. L. Bleche et al., "Enhancing the Kramers–Kronig receiver via dispersion-based spatial diversity," *Opt. Lett.* **45**(13), 3494–3497 (2020).
13. Q. Wu, Y. Zhu, and W. Hu, "Carrier-assisted phase retrieval," *J. Lightwave Technol.* **40**(16), 5583–5596 (2022).
14. Q. Wu et al., "Dual-carrier-assisted phase retrieval for polarization division multiplexing," *J. Lightwave Technol.* **40**(22), 7297–7306 (2022).
15. C. Cuadrado-Laborde et al., "Phase recovery by using optical fiber dispersion," *Opt. Lett.* **39**(3), 598–601 (2014).
16. M. Xiang et al., "Adaptive intensity transformation-based phase retrieval with high accuracy and fast convergence," *Opt. Lett.* **46**(13), 3215–3218 (2021).
17. M. Qiu et al., "Digital subcarrier multiplexing for fiber nonlinearity mitigation in coherent optical communication systems," *Opt. Express* **22**(15), 18770–18777 (2014).
18. P. Poggiolini et al., "Analytical and experimental results on system maximum reach increase through symbol rate optimization," *J. Lightwave Technol.* **34**(8), 1872–1885 (2016).
19. M. Xiang et al., "Hardware-efficient blind frequency offset estimation for digital subcarrier multiplexing signals," *Opt. Express* **29**(13), 19879–19890 (2021).
20. F. P. Guiomar et al., "Frequency-domain hybrid modulation formats for high bit-rate flexibility and nonlinear robustness," *J. Lightwave Technol.* **36**(20), 4856–4870 (2018).
21. M. Xiang et al., "Filtering tolerant digital subcarrier multiplexing system with flexible bit and power loading," in *Opt. Fiber Commun. Conf.*, Optical Society of America, p. W4A.7 (2017).
22. H. Sun et al., "800G DSP ASIC design using probabilistic shaping and digital sub-carrier multiplexing," *J. Lightwave Technol.* **38**(17), 4744–4756 (2020).

23. I. Fatadin and S. J. Savory, "Impact of phase to amplitude noise conversion in coherent optical systems with digital dispersion compensation," *Opt. Express* **18**(15), 16273–16278 (2010).
24. M. Malekiha, I. Tselniker, and D. V. Plant, "Chromatic dispersion mitigation in long-haul fiber-optic communication networks by sub-band partitioning," *Opt. Express* **23**(25), 32654–32663 (2015).
25. M. S. Faruk and K. Kikuchi, "Adaptive frequency-domain equalization in digital coherent optical receivers," *Opt. Express* **19**(13), 12789–12798 (2011).
26. L. Jiang et al., "Fast and adaptive chromatic dispersion compensation scheme for digital coherent systems utilizing two-stage estimation," *Opt. Express* **23**(12), 16177–16183 (2015).

Biographies of the authors are not available.